

# A Contrast-Agnostic Method for Ultra-High Resolution Claustrum Segmentation

Chiara Mauri<sup>a,b,\*</sup>, Ryan Fritz<sup>a</sup>, Jocelyn Mora<sup>a</sup>, Benjamin Billot<sup>c</sup>, Juan Eugenio Iglesias<sup>a,b,c,d</sup>, Koen Van Leemput<sup>e</sup>, Jean Augustinack<sup>a,b</sup>, Douglas N Greve<sup>a,b</sup>

<sup>a</sup>Department of Radiology, Athinoula A. Martinos Center for Biomedical Imaging, Massachusetts General Hospital, Charlestown, MA, USA

<sup>b</sup>Department of Radiology, Harvard Medical School, Boston, MA USA

<sup>c</sup>MIT Computer Science & Artificial Intelligence Laboratory, Cambridge, MA USA

<sup>d</sup>UCL Centre for Medical Image Computing, London, United Kingdom

<sup>e</sup>Department of Neuroscience and Biomedical Engineering, Aalto University, Espoo, Finland

## Abstract

The claustrum is a band-like gray matter structure located between putamen and insula whose exact functions are still actively researched. Its sheet-like structure makes it barely visible in *in vivo* Magnetic Resonance Imaging (MRI) scans at typical resolutions and neuroimaging tools for its study, including methods for automatic segmentation, are currently very limited. In this paper, we propose a contrast- and resolution-agnostic method for claustrum segmentation at ultra-high resolution (0.35 mm isotropic); the method is based on the SynthSeg segmentation framework (Billot et al., 2023), which leverages the use of synthetic training intensity images to achieve excellent generalization. In particular, SynthSeg requires only label maps to be trained, since corresponding intensity images are synthesized on the fly with random contrast and resolution. We trained a deep learning network for automatic claustrum segmentation, using claustrum manual labels obtained from 18 ultra-high resolution MRI scans (mostly *ex vivo*). We demonstrated the method to work on these 18 high resolution cases (Dice score = 0.632, mean surface distance = 0.458 mm, and volumetric similarity = 0.867 using 6-fold Cross Validation (CV)), and also on *in vivo* T1-weighted MRI scans at typical resolutions ( $\approx 1$  mm isotropic). We also demonstrated that the method is robust in a test-retest setting and when applied to multimodal imaging (T2-weighted, Proton Density and quantitative T1 scans). To the best of our knowledge this is the first accurate method for automatic ultra-high resolution claustrum segmentation, which is robust against changes in contrast and resolution. The method is released at [https://github.com/chiara-mauri/claustrum\\_segmentation](https://github.com/chiara-mauri/claustrum_segmentation) and as part of the neuroimaging package Freesurfer (Fischl, 2012).

**Keywords:** Claustrum, Segmentation, *ex vivo* MRI, CNN, Contrast and Resolution invariance, Synthetic images

## 1. Introduction

The claustrum is a thin sheet-like subcortical gray matter structure, which is located between insular cortex and putamen, surrounded by the white matter of the capsule. It is a still actively researched structure, with uncertainty about its exact borders (Mathur, 2014). It includes a thin dorsal part and a thicker ventral portion that displays fragmented components known as “fingers” or “puddles” (Mathur, 2014; Coates and Zaretskaya, 2024; Remedios et al., 2010). While earlier studies measured a volume of around 800 mm<sup>3</sup> on each hemisphere (Kapakin, 2011; Milardi et al., 2015), more recent investigations using high-resolution imaging reported a much larger volume (ranging from 1,243 mm<sup>3</sup> to 2,074 mm<sup>3</sup> on a single hemisphere (Calarco et al., 2023; Coates and Zaretskaya, 2024; Kang et al., 2020)).

The claustrum has been shown to have the highest connectivity in the brain per volume unit (Torgerson et al., 2015), with vast anatomical connections to almost all cortical areas (Baizer et al., 2014; Coates et al., 2023; Crick and Koch, 2005;

Smith et al., 2020; Dillingham et al., 2017), including temporal (Rodríguez-Vidal et al., 2024), motor (Goll et al., 2015), somatosensory (Goll et al., 2015), visual (Goll et al., 2015; Rodríguez-Vidal et al., 2024; Milardi et al., 2015), auditory (Goll et al., 2015; Milardi et al., 2015), limbic (Goll et al., 2015; Smith et al., 2019; Torgerson et al., 2015), associative (Goll et al., 2015), sensorimotor (Rodríguez-Vidal et al., 2024; Milardi et al., 2015) and prefrontal cortices (Goll et al., 2015; Rodríguez-Vidal et al., 2024; Milardi et al., 2015; Brown et al., 2017), and language areas (Rodríguez-Vidal et al., 2024). It has also been shown to be highly interconnected with various subcortical structures (Goll et al., 2015; Dillingham et al., 2017), including basal ganglia and amygdala (Rodríguez-Vidal et al., 2024; Milardi et al., 2015). Besides its wide structural connectivity, claustrum functions have also been object of interest, with hypotheses about its role in consciousness (Smythies et al., 2012; Torgerson et al., 2015; Chau et al., 2015) and conscious percepts (Crick and Koch, 2005), multisensory integration (Mathur, 2014; Banati et al., 2000; Hadjikhani and Roland, 1998; Naghavi et al., 2007), fluency heuristic decisions (Volz et al., 2010), cognitive control (Madden et al., 2022; Krimmel et al., 2019; White et al., 2018), task switching (Krimmel et al., 2019; Mathur, 2014), saliency detection (Mathur, 2014;

\*Corresponding author

Email address: [cmauri@mgh.harvard.edu](mailto:cmauri@mgh.harvard.edu) (Chiara Mauri)

Rodríguez-Vidal et al., 2024; Remedios et al., 2014), attention (Goll et al., 2015; Brown et al., 2017; Smith et al., 2020; Atlan et al., 2018; Mathur, 2014) and salience-guided attention (Smith et al., 2019, 2020; Terem et al., 2020). Additionally, other studies suggested that the claustrum may regulate cortical excitability (Atilgan et al., 2022), modulate cortical down-states during sleep (Smith et al., 2020), and it may be involved in the processing of visual sexual stimuli (Redouté et al., 2000) and in mental preparation leading to successful problem solving (Tian et al., 2011). However, there is still no clear consensus about its functions, with some contradictory results and many open questions (Mathur, 2014; Remedios et al., 2010; Atilgan et al., 2022; Coates et al., 2023; Dillingham et al., 2017; Baizer et al., 2014).

Attention has also been drawn to the possible involvement of claustrum in a variety of neurological disorders (Nikolenko et al., 2021; Benarroch, 2021), such as autism (Wegiel et al., 2015; Davis, 2008), Parkinson’s disease (Sitte et al., 2017; Sener, 1998; Kalaitzakis et al., 2009; Arrigo et al., 2019), schizophrenia (Cascella et al., 2011; Cascella and Sawa, 2014; Bernstein et al., 2016), major depressive disorder (Bernstein et al., 2016), Wilson’s disease (Sener, 1993, 1998), Alzheimer’s disease (Venneri and Shanks, 2014; Bruen et al., 2008), Lewy body dementia (Kalaitzakis et al., 2009; Yamamoto et al., 2007), epilepsy (Silva et al., 2018; Meletti et al., 2015), seizures (Zhang et al., 2001; Wada and Kudo, 1997), delusional states (Patru and Reser, 2015), disruption of consciousness (Koubeissi et al., 2014) and asphyxia (Sener, 1998). However, these findings need to be corroborated by further investigations, with some of these studies suffering from small sample sizes and many aspects yet to be explored.

It is therefore of great interest to further study the claustrum and its functions, and MRI represents a valuable, non-invasive technique for this purpose, with excellent soft tissue contrast. However, difficulties in the study of claustrum arise from its thin shape, making it hard to see in *in vivo* MRI scans at typical resolutions and posing many challenges for both manual labeling and automatic segmentation of the structure. Neuroimaging tools for the study of claustrum are currently very limited. The majority of structural brain atlases for instance do not include claustrum, with the exceptions of a few histological atlases (Ding et al., 2016; Mai et al., 2015; Casamitjana et al., 2024; Ewert et al., 2018; Calarco et al., 2023, 2024). Recently, rigorous protocols for claustrum manual labeling, including both its dorsal and ventral components, have been developed using high-resolution *in vivo* (Kang et al., 2020) and *ex vivo* (Coates and Zaretskaya, 2024) MRI images. However, manual labeling is a time-consuming process which requires domain expertise - even more so for a thin challenging structure like claustrum - and the protocols developed on high-resolution images might not be applicable at lower resolutions. Therefore, it is currently of great interest to develop a reliable method for automatic claustrum segmentation, as crucial step towards a better understanding of the structure and its functions. Such method could also be possibly used for *post hoc* correction of automatic segmentations of the surrounding area, where the putamen is sometimes overlabeled to include parts of the external capsule

and claustrum (Perlaki et al., 2017; Dewey et al., 2010) - in particular for Bayesian segmentation methods which have been very popular in neuroimaging - yielding a potential bias into subsequent region of interest (ROI) analysis.

A few approaches have been proposed in the literature for automatic claustrum segmentation: Berman et al. (2020) used an intensity-based approach on T1- and T2-weighted *in vivo* scans at 0.7 mm isotropic resolution, with k-means clustering employed to separate claustrum from white matter, in a region of interest detected through anatomical landmarks. Brun et al. (2022) adopted a single atlas segmentation approach: It created a brain atlas of claustrum at 0.5 mm isotropic, by registering together 7T T1-weighted *in vivo* scans of multiple subjects and then manually labeling the claustrum in the resulting template. The atlas was then deformed into subject spaces to obtain claustrum segmentation on new cases. Similarly, Coates and Zaretskaya (2024) and Coates et al. (2023) manually labeled the claustrum on a single ultra-high resolution *ex vivo* MRI image (0.1 mm isotropic), and then nonlinearly registered it on unseen *in vivo* scans to yield automatic segmentations. Finally, Albishri et al. (2022) and Li et al. (2021) trained neural networks based on 2D U-Net architectures (Ronneberger et al., 2015) to segment claustrum on T1- and/or T2-weighted *in vivo* scans at 0.7 mm isotropic and 1 mm isotropic resolution respectively, while Neubauer et al. (2022) extended the model from Li et al. (2021) to neonatal brains using transfer learning. However, these approaches suffer from some shortcomings: Berman et al. (2020) achieves low performances and includes only the dorsal portion of the claustrum, Brun et al. (2022) and Coates and Zaretskaya (2024) do not quantify segmentation accuracy, and Albishri et al. (2022) and Li et al. (2021) are difficult to generalize to unseen datasets. In particular, the latter is a limitation of many supervised Convolutional Neural Networks (CNNs), whose generalization ability is hampered by the huge variability in acquisition protocols and sequences across datasets, leading often to the need of fine-tuning or re-training the method before it can be applied to a new domain.

In this paper we propose a novel approach to claustrum segmentation which addresses these shortcomings: We manually labeled claustrum on ultra-high resolution (0.1-0.25 mm isotropic) *ex vivo* and *in vivo* images where claustrum is clearly visible. Then, as *ex vivo* and *in vivo* have different contrasts, we trained a contrast- and resolution-agnostic deep learning network to automatically segment the claustrum. Because of the contrast- and resolution-independent nature of the network, we can also apply this method to *in vivo* datasets at standard ( $\approx 1$  mm isotropic) resolution of any contrast, which is a scenario of interest in many applications. The proposed method is based on SynthSeg (Billot et al., 2023), a segmentation framework that only requires a set of label maps to be trained; no real intensity scans are needed since all training intensity images are synthesized from the labels. In particular, a 3D U-Net (Ronneberger et al., 2015) is trained on a heavily augmented version of given labels, and on corresponding intensity images that are synthesized on the fly with random contrast and resolution, making the automatic segmentation insensitive to contrast and resolution. The use of synthetic images has been widely leveraged

in various neuroimaging applications (Billot et al., 2023; Hoffmann et al., 2021; Iglesias et al., 2021, 2023; Hoopes et al., 2022), and it allows the network to have a rich training environment overlooking idiosyncrasies of a specific training dataset and yielding state-of-the-art generalization (Billot et al., 2023).

The use of this contrast- and resolution-agnostic method yields the following advantages: (1) We can leverage during training ultra-high resolution labels from *ex vivo* scans that capture both dorsal and ventral claustrum, then apply the method to segment all claustrum components in *in vivo* images at typical resolutions. (2) It allows the method to achieve state-of-the-art generalization across different *in vivo* datasets of the same modality, regardless of the specific scanner and acquisition protocol. (3) It allows to segment claustrum in *in vivo* images of any contrast and resolution (such as T1-weighted, T2-weighted, proton density, quantitative T1). To the best of our knowledge this is the first method for automatic high-resolution claustrum segmentation that yields accurate segmentation across all of claustrum and displays excellent generalization. The method is released at [https://github.com/chiera-mauri/claustrum\\_segmentation](https://github.com/chiera-mauri/claustrum_segmentation), as well as in the neuroimaging software FreeSurfer (Fischl, 2012).

## 2. Data

To develop the proposed claustrum segmentation method, we used ultra-high resolution MRI scans of 15 *ex vivo* samples and one *in vivo* T1-weighted scan (0.1-0.25 mm isotropic), whose details are displayed in Table 1, achieving a total of 18 hemispheres (12 left and 6 right hemispheres). These data were used to obtain manual labels of claustrum and to subsequently train a SynthSeg segmentation method, as will be explained in Sec. 3.

We also considered several *in vivo* datasets acquired at typical *in vivo* resolutions, to test the segmentation method in this scenario. In particular, we employed:

- The IXI dataset<sup>1</sup>, which is composed of T1-weighted scans of 581 healthy subjects spanning the whole adulthood (20-86 years old), with resolution  $0.94 \times 0.94 \times 1.20$  mm. This dataset has a mixture of 1.5T and 3T scans from Philips and GE scanners.
- The Miriad dataset (Malone et al., 2013), which contains repeated T1-weighted scans of 46 subjects with mild-moderate Alzheimer’s disease (AD) (mean age  $69.4 \pm 7.1$  years) and of 23 healthy controls (mean age  $69.7 \pm 7.2$  years), acquired by the same radiographer with the same scanner and sequences. The data resolution is  $0.94 \times 0.94 \times 1.50$  mm. For each subject, we used the first two scans, which were taken on average 16 days apart from each other.
- The FreeSurfer Maintenance (FSM) dataset (Greve and Fischl, 2024), which is composed by multimodal images of 39 subjects. Specifically, all subjects in the dataset have a

T1-weighted MPRAGE scan, 36 subjects also have a Proton Density (PD) and a quantitative T1 (qT1) scan from an MP2RAGE (Marques et al., 2010), and 31 subjects have a T2-weighted scan as well (with resolution 1 mm isotropic for all modalities). For 36 subjects, the PD and qT1 were used to synthesize MPRAGE images acquired with different inversion times (TI) with resolution 1 mm isotropic via steady-state Bloch equations (Marques et al., 2010).

## 3. Method

### 3.1. Claustrum manual labeling

The claustrum was manually annotated in all hemispheres presented in Table 1, in the coronal view on every 5th slice using the FreeView software (part of the FreeSurfer software package (Fischl, 2012)), using the following anatomical indications: The claustrum is an extremely thin but tall area of gray matter, which resides within the cortical white matter, broadly located between the putamen medially and insula laterally at its midsection. Two narrow isthmuses of white matter occur on either side of the claustrum, the external capsule medially and the extreme capsule laterally also at its midsection. In the superior direction, the claustrum continues as a narrow strip, extends beyond its midway neighbors (putamen and insula), and ultimately curves toward and hugs the superior cortical gyri. The superior curve of the claustrum points laterally in respective frontal or parietal lobes. In the inferior direction, the claustrum fans out into divided finger-lets. The inferior (or ventral) claustrum occupies a greater territory than the superior portion (which does not expand out at the corona radiata). However, the ventral claustrum is not restrained by the narrow zone near the internal capsule areas and expands ventrally in the temporal stem white matter.

Following these anatomical indications, labels were drawn in Freeview using the voxel edit and polyline tools with a brush size of 1 or 2 voxels, depending on claustrum thickness, followed by filling in the structure. Subsequently, claustrum labels in the remaining slices were obtained with SmartInterpol (Atzeni et al., 2018), a software that exploits a combination of label fusion and convolutional neural networks to transfer the existing labels to the slices without annotations. SmartInterpol has the advantage of reducing the burden of manual tracing, and providing labels that vary smoothly across slices, which is hard to obtain with manual labeling only. After applying SmartInterpol, the segmentation in each slice was cross-checked against contiguous slices, with axial plane and 3D views to confirm proper labeling, and adjustments were made to ensure continuity and anatomical accuracy. Fig. 1 shows an example of an *ex vivo* hemisphere and the corresponding claustrum manual label that we obtained with this procedure. We observe that the label includes both dorsal and ventral portions of the structure, with the latter displaying the characteristic “fingers” in the coronal view.

To assess inter-rater variability, which can be later compared to the performances of the automatic segmentation method, we had three cases (samples 4, 14, and 15 from Table 1) labeled by two different raters independently, following the protocol described above.

<sup>1</sup><http://brain-development.org/ixi-dataset/>

Sample	<i>In vivo/ex vivo</i>	Age	Sex	Field of view (FoV)	PMI (hours)	Brain weights (grams)	MRI resolution (mm, isotropic)
1	<i>ex vivo</i>	78	M	left hemisphere	24	1,320	0.12
2	<i>ex vivo</i>	75	F	left hemisphere	15	1,140	0.12
3 (Costantini et al., 2023)	<i>ex vivo</i>	79	M	left hemisphere	15	1,200	0.15
4	<i>ex vivo</i>	70	F	left hemisphere	23	1,103	0.12
5	<i>ex vivo</i>	73	F	right hemisphere	23	1,500	0.15
6	<i>ex vivo</i>	62	M	left hemisphere	16	1,350	0.15
7	<i>ex vivo</i>	60	F	left hemisphere	2	1,380	0.15
8	<i>ex vivo</i>	75	M	right hemisphere	24	1,310	0.12
9	<i>ex vivo</i>	60	M	left hemisphere	21	1,310	0.12
10	<i>ex vivo</i>	81	M	left hemisphere	6	1,270	0.12
11	<i>ex vivo</i>	61	M	right hemisphere	23	1,310	0.12
12	<i>ex vivo</i>	52	F	left hemisphere	15	1,250	0.12
13 (Edlow et al., 2019)	<i>ex vivo</i>	58	F	whole brain	14	1,210	0.10
14	<i>ex vivo</i>	57	F	left hemisphere	24	1,215	0.12
15	<i>ex vivo</i>	48	M	right hemisphere	?	?	0.12
16 (Lüsebrink et al., 2017)	<i>in vivo</i>	34	M	whole brain	-	-	0.25

Table 1: Demographics of the ultra high-resolution MRI scans used for manual labeling of claustrum. None of the *ex vivo* cases had neurological disorders prior to death, and the *in vivo* scan is from a healthy subject. Some information about sample 15 were not available. PMI = postmortem interval.

### 3.2. Whole field of view (FoV) labels

After obtaining claustrum manual annotations as described in Sec. 3.1, the left hemisphere labels were left-right reversed so that all labels appeared on the right hemisphere. All label volumes were cropped to a FoV of 56 mm per dimension and downsampled to 0.35 mm isotropic voxel size (160 voxels per dimension); this is necessary to accommodate GPU memory during training. SynthSeg training requires dense labels where the whole FoV is annotated, not just claustrum, so we used the default SynthSeg whole brain network (Billot et al., 2023) to segment the surrounding structures - e.g. putamen, cortex, white matter - from the MRI scans (all on the right hemisphere, downsampled to 0.35 mm isotropic), and then cropped the resulting segmentations with the same FoV as the manual labels. The manual claustrum labels were then superimposed on the SynthSeg segmentations; all voxels adjacent to claustrum were forced to be white matter to assure that white matter appeared between claustrum and other structures (such as putamen). These final labels will be used for training the segmentation model. Fig. 2 shows an example of a final label, including both claustrum and surrounding structures.

### 3.3. Training the automatic segmentation method

We trained SynthSeg<sup>2</sup> on the labels described in Sec. 3.2 to segment claustrum and other structures in the ROI (we will show only claustrum segmentations in the remainder). In particular, SynthSeg performs a heavy spatial augmentation of the given labels with both affine and nonlinear diffeomorphic transformation, to enrich the training environment. Synthetic intensity images are then generated, conditioned on the given labels,

by sampling random intensities via a Gaussian Mixture Model. A set of common image augmentations is also applied, with the following order: bias field, intensity normalization, gamma transform, Gaussian smoothing and downsampling (to simulate different random lower resolutions). The synthetic intensity images are then upsampled back to the labels resolution (0.35 mm isotropic in our case) so that the network learns to yield crisp high resolution segmentations, irrespective of the simulated voxel size. A U-Net model (Ronneberger et al., 2015) is trained on these labels-intensities pairs, with the label augmentation and the intensity images generation performed on the fly, so that the network is exposed to more variability.

We first conducted some pilot experiments to determine the optimal configuration of architecture and synthesis hyperparameters for claustrum segmentation (the configuration adopted in Billot et al. (2023) was optimized for whole brain segmentation at 1 mm). Compared to the baseline configuration in Billot et al. (2023), we tweaked different architecture characteristics (such as kernel size, number of levels, number of features, learning rate, batch size, weights attributed in the loss to different structures), and some SynthSeg-specific features (such as grouping of structures in the Gaussian Mixture Model, resolution of synthetic data and hyperparameters of the prior for the amount of rotation and deformation in the labels augmentation, for the Gaussian Mixture Model, and for the gamma transform in the image synthesis). For each modification to the baseline setting, we trained a model for 100 epochs on 12 cases, and we tested it on 3 validation cases. We found that none of these changes yielded a significant improvement in performance (results not shown). We therefore selected the same architecture as in Billot et al. (2023), given by a 3D U-Net with 5 levels, 2 convolutions per level with kernel size 3x3x3, soft Dice Loss, a learning rate of  $10^{-4}$ , and a batch size of 1, and the default synthesis parameters, except for one modification in the image

<sup>2</sup>We used the training code available at <https://github.com/BBillot/SynthSeg>.

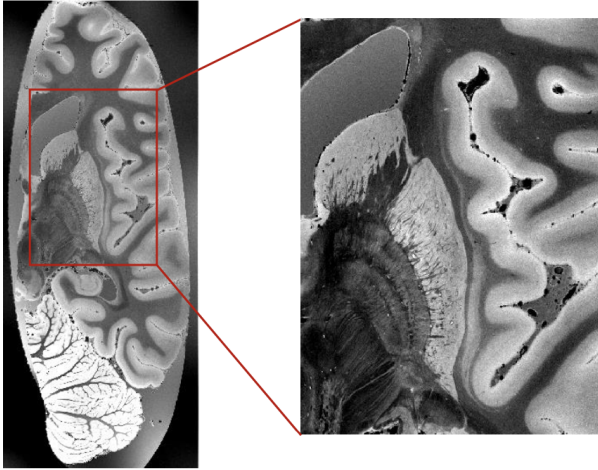


Figure 1: First row: Example of an *ex vivo* hemisphere (axial view), where a cropped region around claustrum is highlighted. Note that the contrast between claustrum and white matter fades in the anterior end of claustrum, raising challenges in the delineation of the structure. Middle row: Axial (left), coronal (middle) and sagittal (right) view of the same hemisphere, cropped around claustrum, with the manual label overlaid. The coronal view shows that the label includes both the thinner dorsal claustrum, which ultimately wraps around the superior cortical gyri (yellow arrow), and the wider ventral portion, which displays the characteristic “fingers” (red arrow). Bottom row: 3D rendering of the claustrum manual label of the same case, shown from two different angles. Note that the structure has only one connected component and that the fragmented look of the ventral “fingers” appears only in 2D views.

synthesis: We added random voxel-wise Gaussian noise when generating synthetic image intensities, since we found that it crucially increased the robustness of the method (see Appendix B).

With this selected configuration, we then trained the model using 6-fold Cross-Validation (CV) to test the performance of the method: We split the data into a training set of 12 subjects, a validation set and a test set of 3 images each, and we repeated

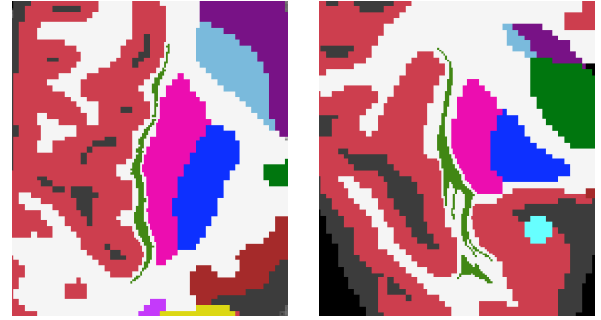


Figure 2: Example of axial (left) and coronal (right) view of a label map, obtained by overimposing the claustrum manual label to the automatic segmentation of surrounding structures, which will be used to train the SynthSeg segmentation model.

the procedure 6 times so that every subject appeared in the test set exactly once. For each split, we trained the model for 100 epochs (500,000 training steps). The validation set was used to determine the best epoch - i.e., the epoch that yielded the best validation Dice score (see Appendix A) for claustrum - which was then used to make predictions on the test subjects.

To apply the method to a new image (for validation and testing in the CV and in all experiments in the remainder), we used the following procedure. We first needed a final step in the processing of the 18 high-resolution data: We non-linearly registered each intensity image to MNI152 using the contrast-insensitive SynthMorph (Hoffmann et al., 2021), and then mapped the claustrum manual labels for all 18 subjects in MNI152 space using this transform (resampling them at 0.35 mm isotropic). We then created a simple prior probabilistic atlas in MNI152 space that can be used to crop a new image into the proper FoV around the claustrum (it is not otherwise used in the segmentation). In particular, given a new test image, we first register it to MNI152, then map the probabilistic atlas into the native space. Once there, we crop a cube of size 60 mm per dimension around the claustrum prior and upsample to 0.35 mm isotropic to create an image of the appropriate size to feed into the model (note that this FoV is in the native space of the input image). Once the image has been cropped and upsampled, the network is applied to yield a segmentation of claustrum in the (0.35 mm isotropic) native space. The registration to establish the FoV again uses SynthMorph so as to maintain contrast-independence. By default, the registration is affine; non-linear registration can be used but increases the processing time. The purpose of the registration step is just to establish a FoV in the location likely to be around the claustrum and otherwise plays no role in the segmentation itself, so an affine is accurate enough.

Using this method to apply the model to intensity images, we assessed CV performances using Dice score as metric. To compare the obtained results we did the following: (1) We computed the Dice score between labels obtained by two different raters on the same samples (described in Sec. 3.1), to have a measure of inter-rater variability. (2) We applied the pre-trained

method from Albishri et al. (2022)<sup>3</sup> to our 0.25 mm isotropic *in vivo* labeled case (sample 16 in Table 1, downsampled at 0.7 mm isotropic to match the training resolution of their model) and computed the resulting overlap with ground truth using Dice score. We also assessed CV performances in terms of other test metrics (true positive rate, false discovery rate, robust Hausdorff distance, mean surface distance, and volumetric similarity; see Appendix A) and compared the claustrum volumes obtained in the automatic segmentations to the ones in the manual labels.

After assessing performances with CV, we trained a final model on all the 18 available cases for 100 epochs (500,000 training steps). We also developed a procedure to assess segmentation quality in absence of ground truth, and used it to choose an epoch of the final model (based on *in vivo* data), as described in the section below.

### 3.4. Quality assessment of segmentations without ground truth

The nonlinear registration of the manual labels in MNI space described in Sec. 3.3 (which was used to create an atlas of claustrum needed to crop a new intensity image) serves two additional purposes: (1) We can compute Dice statistics between any two pairs of manual labels after nonlinear registration; this allows us to understand the variability of the Dice between manual labels, contingent upon the accuracy of the nonlinear registration. (2) It allows us to compute Dice between the automatic segmentation on a new image and the 18 manual labels as a measure of quality (once that image has been nonlinearly registered to MNI152). Note that this nonlinear registration of the new image is only performed as part of the evaluation; it is not needed to do the segmentation.

To assess the quality of a new segmentation, we therefore nonlinearly registered the automatic segmentation into the MNI152 space using SynthMorph. We then compute the Dice score with all the 18 manual labels in MNI152 space, and then select the maximum Dice score as our quality measure (a low value of this metric might denote a segmentation failure). This metric can also be compared to the counterpart computed on the manual labels, i.e. the maximum Dice score for each manual case obtained from pair-wise comparisons with the other manual labels, which yields a distribution of 18 Dice scores setting a reference for Dice inter-subject variability of claustrum. The quality score for a new image can be automatically generated; this allows us to assess the quality of the segmentation method on very large datasets without having to examine each and every image. In theory, this could be applied to every analysis, but the nonlinear registration from the test subject space to MNI space does substantially increase the execution time, so we only use it for our evaluation of segmentation quality.

As mentioned in the previous section, we trained the final model on all manual labels for 100 epochs, but we still need to pick the best one from those 100. We based the epoch selection on T1-weighted *in vivo* images, in particular on a set of 20 subjects from the IXI dataset. On this validation set, we ran the

automatic segmentation for each epoch and used the nonlinear registration to MNI152 to compute the maximum Dice score with the manual labels as discussed above. We then chose the epoch that had the highest mean maximum Dice on the validation subjects, and used the corresponding model as final segmentation method for the experiments described in the next section.

## 4. Experiments on *in vivo* data

To assess robustness, we applied the final segmentation model to all the 581 *in vivo* images from the IXI dataset, computing the maximum Dice score for every subject, as explained in Sec. 3.4. We then visually inspected the cases with the 50 lowest maximum Dices to investigate the potentially worst segmentation results. The motivation of this procedure is that if the subset of the most suspicious cases generally look good, then we assume that the rest of the cases also look good without having to examine each one. Note that a low value of maximum Dice score metric does not always denote a segmentation failure - it could also be caused by a registration issue. This does not affect our quality control procedure, since the metric is simply used to select the pool of potentially suspicious cases which will be then visually inspected. If a successful segmentation is flagged with a low maximum Dice score due to a registration error, the subject still will pass the visual quality control. We also used claustrum volume in the segmentation as indicator of success or failure and looked at the subjects with the 20 smallest and the 20 largest volumes in the dataset. We then compared the distribution of maximum Dice scores and claustrum volumes obtained on the IXI subjects to the corresponding ones obtained on the manual labels.

In order to assess test-retest robustness of the proposed method, we applied it to repeated scans from the Miriad dataset: We rigidly registered the two time points to a subject-specific template (using Reuter et al. (2012)) - as typically done in longitudinal analysis to avoid bias towards one specific time point - then applied the method to both images (using the same FoV), and computed the Dice score between the two segmentations to quantify the stability of the method.

To test the generalization ability of the method to different modalities, we applied it to multimodal images from the FSM dataset. For each subject, we applied the method to the T1-weighted scan as baseline, and to the T2-weighted, Proton Density and quantitative T1 scans (when available), using the same FoV. We then computed the Dice score between the obtained segmentations and the one computed on the T1-weighted scan, as a measure of robustness. Additionally, for each subject for whom they were available, we applied the method to all synthetic images (using the same FoV) and then computed the Dice score between each segmentation and the one obtained on the image with TI=1,000, which was set as reference. This experiment allows us to test the robustness of the method with respect to different contrasts in a controlled setting as well as its ability to handle different TIs that may be encountered in acquisition of real images.

<sup>3</sup> Available at <https://github.com/AhmedAlbishri/AM-UNET>.

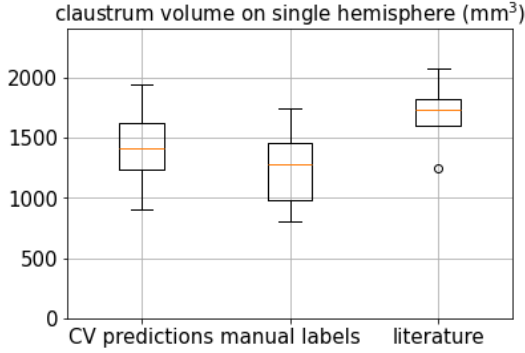


Figure 3: Distribution of claustrum volumes on a single hemisphere in the 18 automatic segmentations obtained with CV, and in the corresponding manual labels. As a reference, we also display values reported in the literature from other studies using high resolution imaging or histology (Coates and Zaretskaya, 2024; Calarco et al., 2023; Kang et al., 2020).

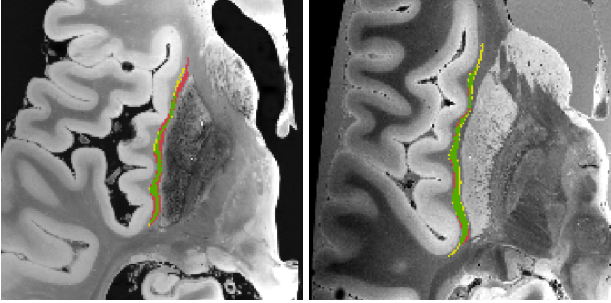


Figure 4: Axial view of predictions obtained with the proposed method, on two test subjects, using two different CV folds. We show in green the true positives, in red the false positives and in yellow the false negatives. Statistics for left case: Dice = 0.616, TPR = 0.700, FDR = 0.450, HD = 1.262 mm, MSD = 0.370 mm, VS = 0.854, predicted volume = 1,239.84 mm<sup>3</sup>, real volume = 923.6 mm<sup>3</sup>. Statistics for right case: Dice = 0.737, TPR = 0.700, FDR = 0.222, HD = 1.443 mm, MSD = 0.332 mm, VS = 0.962, predicted volume = 1,350.03 mm<sup>3</sup>, real volume = 1,457.60 mm<sup>3</sup>.

## 5. Results

The CV results on the 18 high resolution cases are shown in Table 2, reporting an average Dice score of  $0.632 \pm 0.061$ . This compares to an inter-rater variability Dice score of  $0.795 \pm 0.013$  (computed on the samples labeled by two raters), and to a Dice score of 0.299 achieved by the method from Albishri et al. (2022) when applied to our *in vivo* labeled case.

Fig. 3 shows the distribution of claustrum volumes in the CV automatic segmentations, compared to the ones in the manual labels. We obtained an average of  $1,415.35 \pm 260.66$  mm<sup>3</sup> in the automatic vs  $1,253.05 \pm 283.79$  mm<sup>3</sup> in the manual segmentations (a difference of 162 mm<sup>3</sup>, around 13%). Fig. 3 also shows the distribution of claustrum volumes reported in the literature by studies on high resolution imaging or histology (Coates and Zaretskaya, 2024; Calarco et al., 2023; Kang et al., 2020), which displays an average of  $1,692.163 \pm 295.941$  mm<sup>3</sup>.

An example of claustrum segmentation obtained with the proposed method on two test subjects in the CV procedure is shown in Fig. 4. We observe that in one case (left), the

ground truth is very thin and the majority of errors are false positives (Dice score = 0.616, predicted volume 1,239 mm<sup>3</sup> vs real volume of 923 mm<sup>3</sup>). While the other case (right) shows a good agreement between ground truth and prediction, with some false negatives at the boundaries, especially in the anterior and posterior ends where the claustrum is extremely thin (Dice score = 0.737, predicted volume 1,350 mm<sup>3</sup> vs real volume of 1,457 mm<sup>3</sup>).

When we then trained the model on all the 18 high-resolution cases, training took around 7 days on an RTX 8000 GPU. The procedure for identifying the optimal epoch based on the maximum Dice score as described in Sec. 3.4 selected the model of the 19th epoch, which yielded an average maximum Dice score of  $0.580 \pm 0.060$  on the IXI subset used for validation.

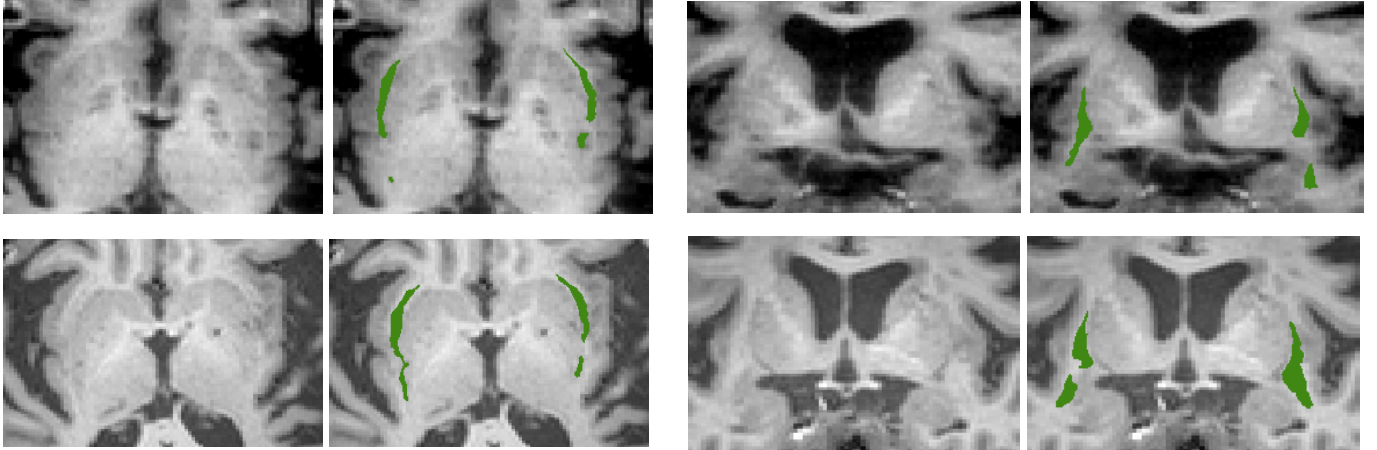
After applying this final segmentation method to all the IXI data and visually inspecting the cases with the 50 lowest maximum Dice scores, and with the 20 smallest and 20 largest volumes, we concluded that the method showed some segmentations errors in around half of the inspected volumes, but it never severely failed. The most common error was to label some part of the putamen as claustrum, especially in its posterior part, or in presence of darker voxels within the putamen, as is shown in Fig. 5. These voxels are likely Vichow-Robins spaces or some kind of lesion. Since the set of examined subjects is expected to include the worst segmentations, we can conclude that the method never critically failed when applied to over 500 subjects from the IXI dataset. Fig. 5 shows the segmentations obtained for the subjects with the two lowest and the two highest maximum Dice scores. We observe that the segmentations with the two lowest scores appear incomplete and overlapping to the putamen at times, especially in presence of darker voxels. On the other end, in the cases with the two highest scores, the segmentations are anatomically accurate and complete, with the claustrum wrapping around the cortex superiorly (in the coronal views).

Additionally, Fig. 6 shows the distribution of maximum Dice scores and claustrum volumes obtained on the IXI subjects, together with the corresponding distributions computed on the manual labels. We obtained an average maximum Dice score of  $0.570 \pm 0.060$  for the IXI dataset and  $0.539 \pm 0.078$  on the manual segmentations. Regarding claustrum volumes, we obtained a mean of  $1,793.92 \pm 259.16$  and  $1,253.05 \pm 283.79$  mm<sup>3</sup> on the IXI subjects and the manual labels respectively, which compare to an average of  $1,692.163 \pm 295.941$  mm<sup>3</sup> of claustrum volumes reported in the literature (Coates and Zaretskaya, 2024; Calarco et al., 2023; Kang et al., 2020).

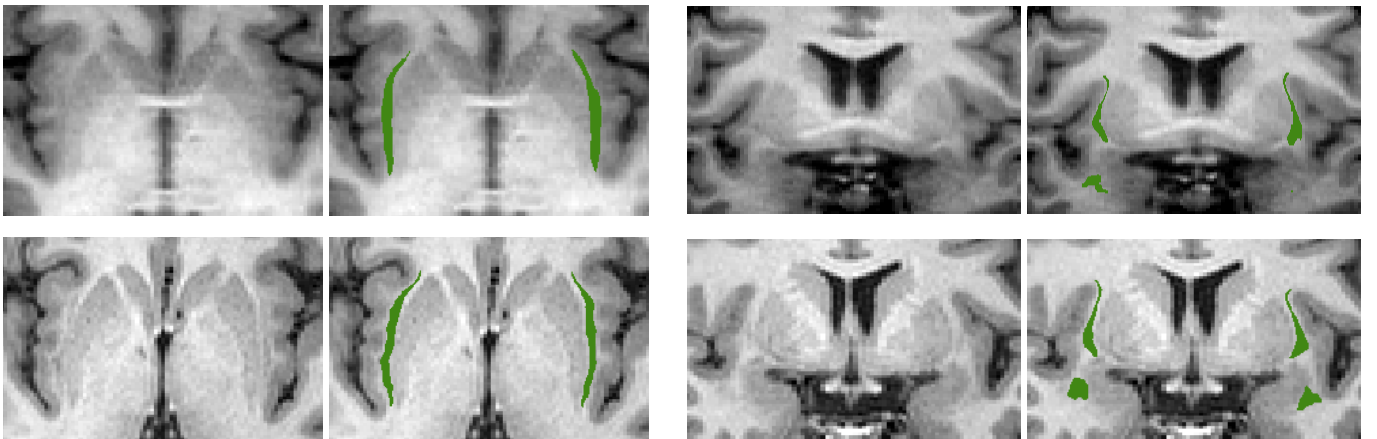
On the Miriad test-retest dataset, we discarded 3 subjects for which the first two sessions scans were unavailable, and other 5 subjects where the rigid registration was inaccurate (for a scale difference in the two images), obtaining 40 AD subjects and 21 healthy controls. On these remaining subjects, we obtained an average Dice score between claustrum segmentations computed on two subsequent scans of  $0.781 \pm 0.068$  ( $0.774 \pm 0.068$  on AD subjects and  $0.796 \pm 0.065$  on healthy controls), denoting a good robustness of the method. Fig. 7 shows an example of the agreement between the segmentations on repeated scans for one AD subject and one healthy control. We observe that the

Dice score	True positive rate (TPR)	False discovery rate (FDR)	Robust Hausdorff distance (HD)	Mean surface distance (MSD)	Volumetric similarity (VS)
$0.632 \pm 0.061$	$0.676 \pm 0.100$	$0.381 \pm 0.119$	$1.824 \pm 0.585$ mm	$0.458 \pm 0.124$ mm	$0.867 \pm 0.092$

Table 2: Results of 6-fold CV on the 18 high-resolution cases. For each test metric, mean and standard deviation across the 18 cases are reported.



(a) Axial (left) and coronal (right) views of the subjects in the IXI dataset with the two lowest maximum Dice scores. First row: Maximum Dice score averaged across hemispheres = 0.362. Second row: Maximum Dice score averaged across hemispheres = 0.415.



(b) Axial (left) and coronal (right) views of the subjects in the IXI dataset with the two highest maximum Dice scores. First row: Maximum Dice score averaged across hemispheres = 0.638. Second row: Maximum Dice score averaged across hemispheres = 0.639.

Figure 5: Claustrum segmentation on subjects from the IXI dataset with the two lowest and the two highest maximum Dice score (averaged across hemispheres).

repeated segmentations display a good overlap, with most of the differences being boundary disputes.

Table 3 shows the average Dice score between segmentations obtained on different modalities of the same subject in the FSM dataset. We observe that the highest average Dice is obtained between quantitative T1 and T1-weighted ( $0.809 \pm 0.044$ ) and lowest obtained between Proton Density and T1-weighted scans ( $0.696 \pm 0.085$ ). Fig. 8 shows images from different modalities of one subject, together with the overlap between the segmentation obtained on these modalities and the one computed on the T1-weighted scan. We note that there is a good agreement, with a few differences at the boundaries.

Fig. 9 shows the Dice score between claustrum segmentations computed on synthesized images with varying TI and the one obtained on TI=1,000, averaged across subjects of the FSM

T2w vs T1w (n=31)	PD vs T1w (n=36)	qT1 vs T1w (n=36)
$0.720 \pm 0.083$	$0.696 \pm 0.085$	$0.809 \pm 0.044$

Table 3: Mean and standard deviation of Dice score between claustrum segmentations computed on T1-weighted (T1w) scans and other modalities (T2-weighted (T2w), Proton Density (PD) and quantitative T1 (qT1)) of the same subject, across all subjects in the FSM dataset. In brackets, the number of subjects that are used to compute the average Dice score.

dataset. As the TI increases, the Dice score initially decreases on average, reaching its minimum at TI=380 with an average value of  $0.676 \pm 0.094$ , and then it increases towards a complete overlap. When averaged across all TI and subjects, the method obtains a Dice score of  $0.873 \pm 0.109$ . Fig. 10 shows synthetic images with varying TI for one subject in the dataset, to-



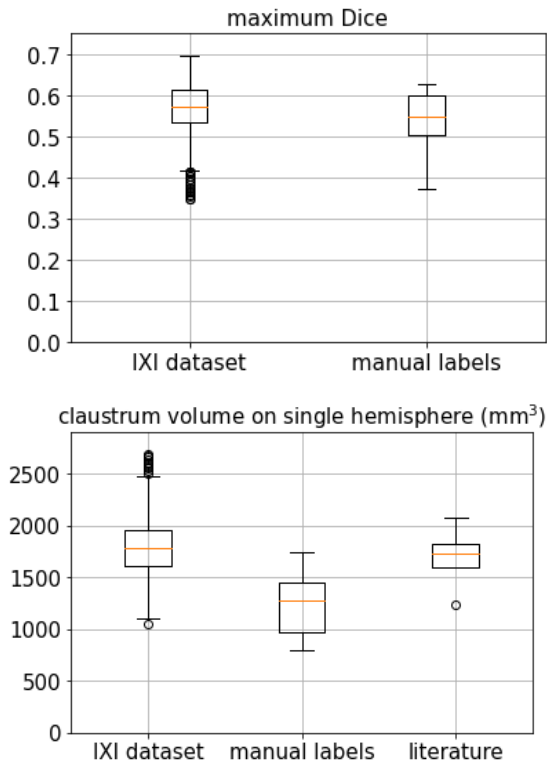


Figure 6: Top: Distribution of maximum Dice scores on the IXI subjects, computed as explained in Sec. 3.4, together with the corresponding distribution obtained on the manual labels. Bottom: Distribution of claustrum volumes on a single hemisphere on the automatic segmentations on IXI subjects, and in the manual labels. As a reference, we also display values reported in the literature from other studies using high resolution imaging or histology (Coates and Zaretskaya, 2024; Calarco et al., 2023; Kang et al., 2020).

gether with the agreement between the segmentations obtained on those images and the one computed on  $TI=1,000$ . We observe that the contrast changes rapidly from  $TI=300$  to  $TI=500$ , and then it varies more smoothly, in line with the Dice changing shown in Fig. 9. In general the subject displays a very good overlap between the segmentations, with the most differences obtained at  $TI=400$ , in line with the lowest Dice score achieved on average at  $TI=380$  in Fig. 9.

In all these experiments on *in vivo* data, it took around 3 minutes to apply the method on a subject using basic configurations (only the affine registration to MNI152 space to determine the FoV) using a machine with 16 CPUs. The version with the non-linear registration to MNI152 space to do the quality assessment with the maximum Dice took around 10 minutes per subject on the same machine.

## 6. Discussion and conclusion

In this paper we proposed a method based on the SynthSeg framework for ultra-high resolution claustrum segmentation, which is robust against changes in contrast and resolution. To the best of our knowledge this is the first method for automatic claustrum segmentation with these features. The method was

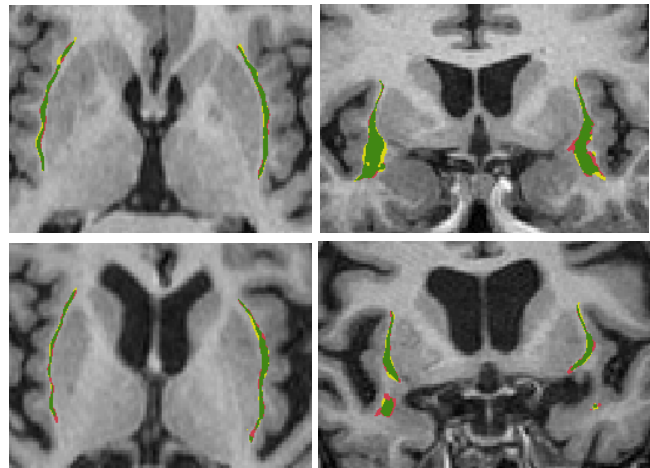


Figure 7: Axial (left) and coronal (right) view of claustrum segmentations obtained on repeated T1-weighted scans of two subjects from the Miriad dataset. In green we show the overlap between the two time points segmentations, in red the voxels in the first time point segmentation that are not included in the second one, and in yellow the voxels in the second time point segmentation that are not included in the first one. Top row: Healthy subject with Dice score between segmentations of 0.836 (averaged across hemispheres). Bottom row: AD subject with Dice score between segmentations of 0.802 (averaged across hemispheres).

designed to exploit ultra-high resolution *ex vivo* images, which display details that are not visible in typical *in vivo* scans, to learn to segment claustrum in all its components. Then, since it is contrast- and resolution- agnostic, the method can be applied to *in vivo* images (whose contrast in general differs from the *ex vivo* scans), of any contrast and resolution.

We assessed the performances of the method using CV on our 18 high-resolution scans, where we obtained a moderate Dice score ( $0.632 \pm 0.061$ ), which might be due to the challenging nature of claustrum segmentation at ultra-high resolution. We also quantified CV performances in terms of other metrics, achieving for instance a mean surface distance of  $0.458 \pm 0.124$  mm, a robust Hausdorff distance of  $1.824 \pm 0.585$  mm, and a volumetric similarity of  $0.867 \pm 0.092$ . The value of our CV Dice score is lower than the inter-rater variability average Dice computed on labels obtained by two different raters on the same samples ( $0.795 \pm 0.013$ ). However the use of SmartInterpol by both raters might have inflated the label similarity. Other studies assessed inter-rater variability for claustrum segmentation, reporting Dice values between 0.67 and 0.83 (Berman et al., 2020; Coates et al., 2023; Coates and Zaretskaya, 2024), while Li et al. (2021) computed an intra-rater variability Dice score of 0.667.

Comparing our Dice score with performances of other available segmentation methods, we observe that Berman et al. (2020) achieved an average Dice score of 0.55, while Brun et al. (2022) and Coates and Zaretskaya (2024) did not quantify their claustrum segmentation accuracy - Coates and Zaretskaya (2024) reported that their own method can be used to *approximate* the claustrum location in typical MRI scans. Only Li et al. (2021) and Albishri et al. (2022) achieved higher Dices (0.718 and 0.82 respectively). In this regard, it is worth noting that our

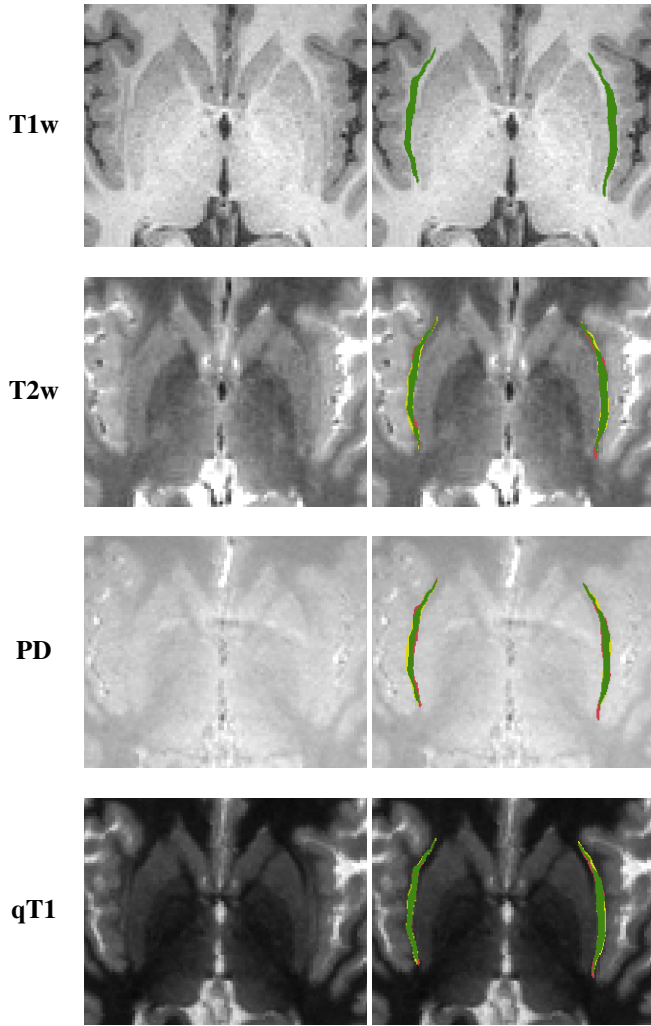


Figure 8: Left: Axial view of different modalities of the same subject from the FSM dataset. Right: Overlap between the segmentation obtained on the given modality and the one computed on the T1w scan. In green, we show the overlap between the two segmentations, in red the voxels that are in the T1w segmentation and that are not included in the other modality one, and in yellow the voxels in the other modality segmentation that are not included in the T1w one. For this subject, Dice scores vs T1w segmentation averaged across hemispheres are 0.800 for T2w, 0.730 for PD and 0.818 for qT1.

results are obtained at much higher resolution, where it might be more challenging to get all the details and nuances of claustrum. Additionally, in general a contrast-agnostic method is expected to perform worse than a supervised CNN that is tested on its training domain, but it gains in ability to generalize. For instance, Albishri et al. (2022)’s Dice score of 0.82 was assessed with 5-fold CV within one homogeneous dataset. When we applied their pre-trained method to our *in vivo* labeled case, the predictions were poor, with a Dice score of 0.299. Besides the change of dataset (with different scanner and image acquisition protocol), differences in image resolution and labeling protocol may also account for the significant decrease in performance.

Importantly, in addition to CV on the 18 high-resolution cases, we demonstrated that the method also works on *in vivo* T1-weighted scans at typical *in vivo* resolutions ( $\approx 1$  mm

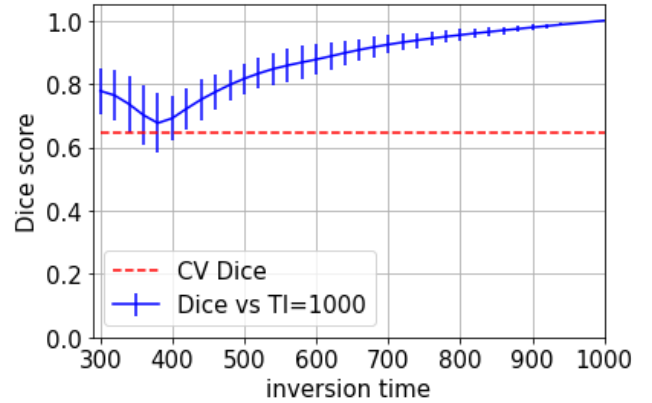


Figure 9: Dice score between claustrum segmentations computed on synthetic images with different TI and the one obtained on TI=1,000, on the FSM dataset. The full line shows the average Dice across all the subjects, and the bars extend to one standard deviation away from the average. The Dice score obtained on average using CV on the high resolution cases is also shown as reference (0.632, see Table 2).

isotropic) from the IXI, Miriad, and FSM datasets, including on subjects with AD. On the IXI data, we assessed segmentation accuracy in absence of ground truth by using the maximum Dice score and claustrum volume as indicators of segmentation success, and we concluded that the method did not severely fail on any subject. Additionally, comparing the maximum Dice scores on the IXI data to the ones computed on the manual labels, we obtained similar values on average ( $0.570 \pm 0.060$  vs  $0.539 \pm 0.078$  respectively), denoting that the automatic claustrum segmentations display anatomically plausible variations. We point out here that IXI is a challenging data set with a very wide subject age range, large voxel size, 1.5T and 3.0T, and two different MRI scanner manufacturers. The success of the claustrum segmentation on 581 subjects from this dataset demonstrates its robustness.

Furthermore, the proposed method was shown to be robust on test-retest scans (average Dice score between two repeated scans of  $0.781 \pm 0.068$ ) and when applied to multimodal images. In particular, it showed a good generalization ability to different modalities, with the lowest overlap obtained between Proton Density and T1-weighted scans ( $0.696 \pm 0.085$ ), probably because of the poor contrast around claustrum in Proton Density images. When using synthetic images to simulate different MPRAGES over a range of TIs, the method showed very good robustness as well (average Dice score across all TIs and subjects of  $0.873 \pm 0.109$ ), with the most differences observed on average at TI=380 (Dice score of  $0.676 \pm 0.094$ ). We point out that the change in contrast over this TI range is extreme (see Fig. 10) and was meant as a stress test on the contrast-agnostic performance of the method. Even over this extreme range, the method still performs very well.

With respect to claustrum volumes computed in our segmentations, in CV results on the high-resolution cases we obtained similar volumes as the manual labels ( $1,415.35 \pm 260.66$  mm<sup>3</sup> in CV segmentations vs  $1,253.05 \pm 283.79$  mm<sup>3</sup> in manual labels; around 13% difference), while on the IXI data, claustrum

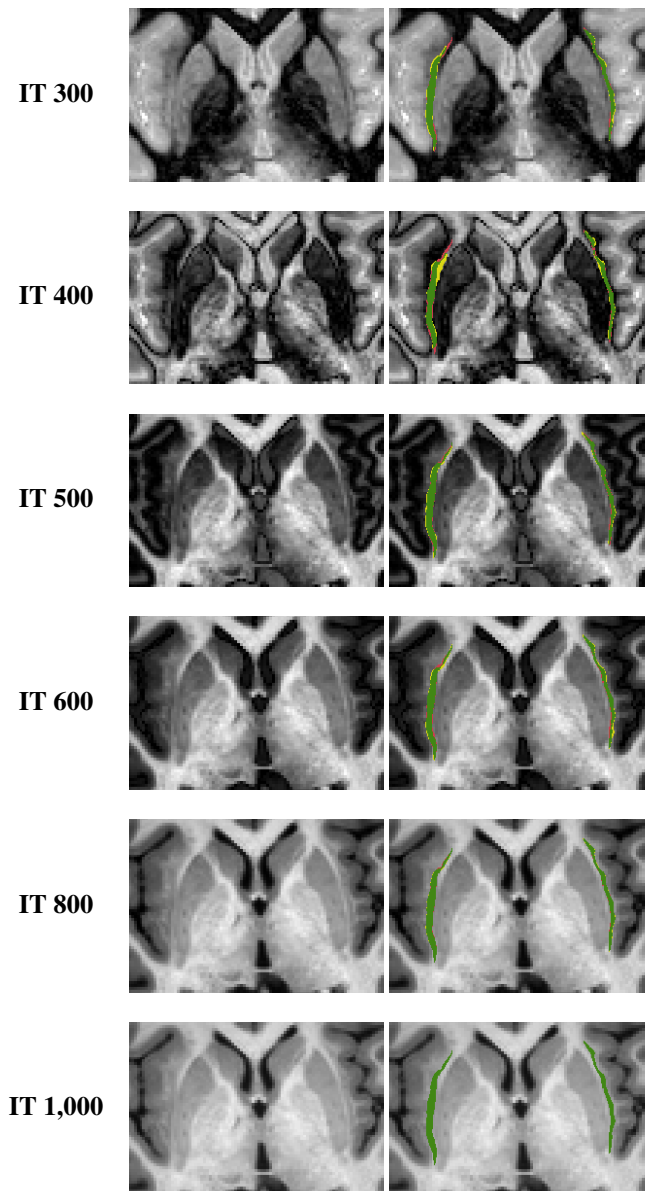


Figure 10: Left: Axial view of synthetic images of one subject from the FSM dataset, obtained with different TI. Right: Overlap between the segmentation obtained on the image with the given TI and the one computed on TI=1,000. In green, we show the overlap between the two segmentations, in red the voxels that are in the segmentation on TI = 1,000 and not in the other TI one, and in yellow the vice versa.

volumes were substantially higher than in the manual segmentations ( $1,793.92 \pm 259.16$  vs  $1,253.05 \pm 283.79$   $\text{mm}^3$  respectively). It is not clear why the IXI volumes are so much higher, but it is likely due to partial volume effects at 1 mm when trying to segment a structure sometimes only 0.5 mm wide. Furthermore, by comparing the volumes in our manual labels to what reported by other claustrum studies using high-resolution imaging or histology, we saw that our manual labels present a lower volume on average: They are in line with what reported by Calarco et al. (2023) ( $1,243$   $\text{mm}^3$ ), but smaller than other investigations (Coates and Zaretskaya, 2024; Kang et al., 2020).

In our experimental design, we cropped the training labels with the claustrum in the center of the FoV. This is a common choice in image segmentation tasks, although not ideal since it can lead to shortcut learning where the network learns not to locate claustrum at the borders (Lin et al., 2024). However, in practice this choice does not hamper our results since at test time we have a consistent way of centering the FoV around claustrum. Additionally, in our experiments we used two different methods for model validation: in CV we maximized the Dice score on labeled images (mostly *ex vivo*), while in the final model we wanted to use all available labeled data for training; therefore we maximized the average maximum Dice score, as quality metric in absence of ground truth, on a subset of IXI images (*in vivo* T1-weighted scans). These choices were made for the lack of a labeled heterogeneous validation set with different contrasts and resolutions that ideally should be used for SynthSeg validation. While on one hand the method may then be biased towards the specific contrast and resolution of validation images, on the other hand we showed that the final model performs well on a diverse set of contrasts.

As a limitation of the current work, we should mention that, while the method is resolution-agnostic with no theoretical constraint on the voxel size, in practice it will need to be run on good quality images to achieve satisfying results (with voxel size at least 1-1.5 mm and without excessive noise). If the resolution or image quality is insufficient, part or all claustrum may not be visible. In absence of signal, the segmentation will be mostly guessed and the results need to be interpreted with caution. Another limitation is that, despite the extensive hyperparameter tuning that we conducted, the performances achieved with CV on high-resolution data are moderate. As future work, we can explore other ways to improve model performance, such as using a loss function more suitable than Dice loss for thin structures like claustrum (e.g. a distance transform loss or a topology-preserving loss specifically designed for thin structures (Kirchhoff et al., 2024)), or by constraining the image synthesis to have some minimum contrast around claustrum, avoiding cases where the structure might not be visible.

Besides these limitations, the proposed method was able to address shortcomings of existing methods for claustrum segmentation, such as segmenting only the dorsal part of claustrum (Berman et al., 2020) achieving inaccurate or unquantified results (Berman et al., 2020; Brun et al., 2022; Coates and Zaretskaya, 2024), and being difficult to generalize to unseen datasets (Albishi et al., 2022; Li et al., 2021). Thanks to the use of synthetic images during training - with augmented labels and random contrast intensities (Billot et al., 2023) - it was able to successfully segment dorsal and ventral portions of claustrum in T1-weighted scans across multiple datasets, and multimodal images as well, yielding an exceptional generalization. Given the scarcity of neuroimaging tools for the study of claustrum (including methods for its automatic segmentation), the shortcomings of existing methods, and the variety of open questions that are still concerning the structure and its functions, we believe that the proposed method will be a valuable tool for further investigations of claustrum. It will also be potentially useful as *post hoc* correction of automatic segmentations of the surround-

ing area, such as correction of putamen overlabeling (Perlaki et al., 2017; Dewey et al., 2010).

## Acknowledgment

Much of the computation resources required for this research was performed on computational hardware generously provided by the Massachusetts Life Sciences Center (<https://www.masslifesciences.com/>). We would also like to acknowledge support from NIH grants R01NS105820, R01EB023281, R01NS083534, R01AG057672, and R01NS112161, and grants 1RF1MH123195, 1R01AG070988, 1UM1MH130981, and 1RF1AG080371. This project was also supported by the Innovative Health Initiative Joint Undertaking (JU) under grant agreement No 101112153. The JU receives support from the European Union’s Horizon Europe research and innovation programme and COCIR, EFPIA, EuropaBio, MedTech Europe, Vaccines Europe, AB Science SA and Icometrix NV.

## Appendix A. Test metrics

To assess CV performances of the segmentation method, we used the following metrics:

- Dice score: it is a measure of volumetric overlap between two structures A and B, defined as  $\frac{2v(A \cap B)}{v(A) + v(B)}$  where  $v(\cdot)$  represents the volume of a structure.
- True positive rate: it is defined as  $TP / (TP + FN)$ , where  $TP$  = number of true positives,  $FN$  = number of false negatives,  $FP$  = number of false positives.
- False discovery rate: it is defined as  $FP / (FP + TP)$ , where  $TP$  = number of true positives,  $FN$  = number of false negatives,  $FP$  = number of false positives.
- Robust Hausdorff distance: we used Hausdorff distance (Huttenlocher et al., 1993) with 95% percentile.
- Mean surface distance: mean surface distance between two surfaces  $S$  and  $S'$  is defined as  $\frac{1}{n_S + n_{S'}} (\sum_{p \in S} d(p, S') + \sum_{p' \in S'} d(p', S))$  where  $n_S, n_{S'}$  are the number of points on surfaces  $S$  and  $S'$  respectively, and for a given point  $p \in S$  we define the distance from  $S'$  as  $d(p, S') = \min_{p' \in S'} \|p - p'\|_2$ .
- Volumetric similarity: volumetric similarity between two structures A and B is defined as  $1 - \frac{|v(A) - v(B)|}{v(A) + v(B)}$  where  $v(\cdot)$  represents the volume of a structure.

## Appendix B. Increasing the robustness of the method by adding voxel-wise noise

We compared the model with and without adding random voxel-wise Gaussian noise in the synthetic intensity images during training. The noise is added as part of the intensity image

augmentation right after the bias field simulation, in the following way: We sample a standard deviation  $\sigma$  from a uniform distribution  $\sigma \in \mathcal{U}(0, 100)$ , then sample independent voxel-wise Gaussian noise from  $\mathcal{N}(0, \sigma^2)$ , and add it to the intensity image with probability 95%.

For the case with noise, we used the model trained on the first fold of the CV described in Sec. 3.3, following the same procedure for selecting the best epoch (i.e. maximizing the Dice score on the validation set of that fold). We then applied the resulting model to all IXI subjects and computed the maximum Dice score as detailed in Sec. 3.4. We then trained a model on the same CV fold *without* adding noise to the synthetic images, and repeated the same procedure. We obtained an average maximum Dice score on the IXI dataset of  $0.555 \pm 0.050$  for the model with noise, and  $0.490 \pm 0.094$  for the one without noise, which compare to the average maximum Dice on the manual labels of  $0.539 \pm 0.078$ , showing that the model with noise achieves more robust results.

## References

- Albshri, A. A., Shah, S. J. H., Kang, S. S. and Lee, Y. (2022), ‘Am-unet: automated mini 3d end-to-end u-net based network for brain claustrum segmentation’, *Multimedia Tools and Applications* **81**(25), 36171–36194.
- Arrigo, A., Calamuneri, A., Milardi, D., Mormina, E., Gaeta, M., Corallo, F., Lo Buono, V., Chillemi, G., Marino, S., Cacciola, A. et al. (2019), ‘Claustal structural connectivity and cognitive impairment in drug naïve parkinson’s disease’, *Brain Imaging and Behavior* **13**, 933–944.
- Atilgan, H., Doody, M., Oliver, D. K., McGrath, T. M., Shelton, A. M., Echeverria-Altuna, I., Tracey, I., Vyazovskiy, V. V., Manohar, S. G. and Packer, A. M. (2022), ‘Human lesions and animal studies link the claustrum to perception, salience, sleep and pain’, *Brain* **145**(5), 1610–1623.
- Atlas, G., Terem, A., Peretz-Rivlin, N., Sehwat, K., Gonzales, B. J., Pozner, G., Tasaka, G.-i., Goll, Y., Refaeli, R., Zviran, O. et al. (2018), ‘The claustrum supports resilience to distraction’, *Current Biology* **28**(17), 2752–2762.
- Atzeni, A., Jansen, M., Ourselin, S. and Iglesias, J. E. (2018), A probabilistic model combining deep learning and multi-atlas segmentation for semi-automated labelling of histology, in ‘Medical Image Computing and Computer Assisted Intervention–MICCAI 2018: 21st International Conference, Granada, Spain, September 16–20, 2018, Proceedings, Part II 11’, Springer, pp. 219–227.
- Baizer, J. S., Sherwood, C. C., Noonan, M. and Hof, P. R. (2014), ‘Comparative organization of the claustrum: what does structure tell us about function?’, *Frontiers in systems neuroscience* **8**, 117.
- Banati, R. B., Goerres, G. W., Tjoa, C., Aggleton, J. P. and Grasby, P. (2000), ‘The functional anatomy of visual-tactile integration in man: a study using positron emission tomography’, *Neuropsychologia* **38**(2), 115–124.
- Benarroch, E. E. (2021), ‘What is the role of the claustrum in cortical function and neurologic disease?’, *Neurology* **96**(3), 110–113.
- Berman, S., Schurr, R., Atlas, G., Citri, A. and Mezer, A. A. (2020), ‘Automatic segmentation of the dorsal claustrum in humans using in vivo high-resolution mri’, *Cerebral Cortex Communications* **1**(1), tga062.
- Bernstein, H.-G., Ortmann, A., Dobrowolny, H., Steiner, J., Brisch, R., Gos, T. and Bogerts, B. (2016), ‘Bilaterally reduced claustral volumes in schizophrenia and major depressive disorder: a morphometric postmortem study’, *European archives of psychiatry and clinical neuroscience* **266**, 25–33.
- Billot, B., Greve, D. N., Puonti, O., Thielscher, A., Van Leemput, K., Fischl, B., Dalca, A. V., Iglesias, J. E. et al. (2023), ‘Synthseg: Segmentation of brain mri scans of any contrast and resolution without retraining’, *Medical image analysis* **86**, 102789.
- Brown, S. P., Mathur, B. N., Olsen, S. R., Luppi, P.-H., Bickford, M. E. and Citri, A. (2017), ‘New breakthroughs in understanding the role of functional interactions between the neocortex and the claustrum’, *Journal of Neuroscience* **37**(45), 10877–10881.

- Bruen, P. D., McGeown, W. J., Shanks, M. F. and Venneri, A. (2008), 'Neuroanatomical correlates of neuropsychiatric symptoms in alzheimer's disease', *Brain* **131**(9), 2455–2463.
- Brun, G., Testud, B., Girard, O. M., Lehmann, P., de Rochefort, L., Besson, P., Massire, A., Ridley, B., Girard, N., Guye, M. et al. (2022), 'Automatic segmentation of deep grey nuclei using a high-resolution 7t magnetic resonance imaging atlas—quantification of t1 values in healthy volunteers', *European Journal of Neuroscience* **55**(2), 438–460.
- Calarco, N., Kashyap, S. and Uludağ, K. (2023), Establishing an MRI reference for the human claustrum. Poster presented at OHBM 2023, Montreal.
- Calarco, N., Kedo, O., Bludau, S., Herold, C., Uludag, K. and Amunts, K. (2024), Cytoarchitectonic mapping and probabilistic atlas of the human claustrum. Poster presented at OHBM 2024, Seoul.
- Casamitjana, A., Mancini, M., Robinson, E., Peter, L., Annunziata, R., Althonayan, J., Crampsie, S., Blackburn, E., Billot, B., Atzeni, A. et al. (2024), 'A next-generation, histological atlas of the human brain and its application to automated brain mri segmentation', *bioRxiv* pp. 2024–02.
- Cascella, N. G., Gerner, G. J., Fieldstone, S. C., Sawa, A. and Schretlen, D. J. (2011), 'The insula-claustrum region and delusions in schizophrenia', *Schizophrenia Research* **133**(1-3), 77–81.
- Cascella, N. G. and Sawa, A. (2014), The claustrum in schizophrenia, in 'The claustrum', Elsevier, pp. 237–243.
- Chau, A., Salazar, A. M., Krueger, F., Cristofori, I. and Grafman, J. (2015), 'The effect of claustrum lesions on human consciousness and recovery of function', *Consciousness and Cognition* **36**, 256–264.
- Coates, A., Linhardt, D., Windischberger, C., Ischebeck, A. and Zaretskaya, N. (2023), 'High-resolution 7t fmri reveals the visual sensory zone of the human claustrum', *bioRxiv* pp. 2023–09.
- Coates, A. and Zaretskaya, N. (2024), 'High-resolution dataset of manual claustrum segmentation', *Data in Brief* **54**, 110253.
- Costantini, I., Morgan, L., Yang, J., Balbastre, Y., Varadarajan, D., Pesce, L., Scardigli, M., Mazzamuto, G., Gavryusev, V., Castelli, F. M. et al. (2023), 'A cellular resolution atlas of broca's area', *Science Advances* **9**(41), eadg3844.
- Crick, F. C. and Koch, C. (2005), 'What is the function of the claustrum?', *Philosophical Transactions of the Royal Society B: Biological Sciences* **360**(1458), 1271–1279.
- Davis, W. (2008), *The claustrum in autism and typically developing male children: a quantitative MRI study*, Brigham Young University.
- Dewey, J., Hana, G., Russell, T., Price, J., McCaffrey, D., Harezlak, J., Sem, E., Anyanwu, J. C., Guttman, C. R., Navia, B. et al. (2010), 'Reliability and validity of mri-based automated volumetry software relative to auto-assisted manual measurement of subcortical structures in hiv-infected patients from a multisite study', *Neuroimage* **51**(4), 1334–1344.
- Dillingham, C. M., Jankowski, M. M., Chandra, R., Frost, B. E. and O'Mara, S. M. (2017), 'The claustrum: Considerations regarding its anatomy, functions and a programme for research', *Brain and Neuroscience Advances* **1**, 2398212817718962.
- Ding, S.-L., Royall, J. J., Sunkin, S. M., Ng, L., Facer, B. A., Lesnar, P., Guillozet-Bongaarts, A., McMurray, B., Szafer, A., Dolbeare, T. A. et al. (2016), 'Comprehensive cellular-resolution atlas of the adult human brain', *Journal of comparative neurology* **524**(16), 3127–3481.
- Edlow, B. L., Mareyam, A., Horn, A., Polimeni, J. R., Witzel, T., Tisdall, M. D., Augustinack, J. C., Stockmann, J. P., Diamond, B. R., Stevens, A. et al. (2019), '7 tesla mri of the ex vivo human brain at 100 micron resolution', *Scientific data* **6**(1), 244.
- Ewert, S., Plettig, P., Li, N., Chakravarty, M. M., Collins, D. L., Herrington, T. M., Kühn, A. A. and Horn, A. (2018), 'Toward defining deep brain stimulation targets in mni space: a subcortical atlas based on multimodal mri, histology and structural connectivity', *Neuroimage* **170**, 271–282.
- Fischl, B. (2012), 'Freesurfer', *Neuroimage* **62**(2), 774–781.
- Goll, Y., Atlán, G. and Citri, A. (2015), 'Attention: the claustrum', *Trends in neurosciences* **38**(8), 486–495.
- Greve, D. N. and Fischl, B. (2024), 'The FreeSurfer Maintenance Dataset'. OpenNeuro, doi:10.18112/openneuro.ds004958.v1.0.0.
- Hadjikhani, N. and Roland, P. E. (1998), 'Cross-modal transfer of information between the tactile and the visual representations in the human brain: a positron emission tomographic study', *Journal of Neuroscience* **18**(3), 1072–1084.
- Hoffmann, M., Billot, B., Greve, D. N., Iglesias, J. E., Fischl, B. and Dalca, A. V. (2021), 'Synthmorph: learning contrast-invariant registration without acquired images', *IEEE transactions on medical imaging* **41**(3), 543–558.
- Hoopes, A., Mora, J. S., Dalca, A. V., Fischl, B. and Hoffmann, M. (2022), 'Synthstrip: skull-stripping for any brain image', *NeuroImage* **260**, 119474.
- Huttenlocher, D. P., Klanderman, G. A. and Rucklidge, W. J. (1993), 'Comparing images using the hausdorff distance', *IEEE Transactions on pattern analysis and machine intelligence* **15**(9), 850–863.
- Iglesias, J. E., Billot, B., Balbastre, Y., Magdamo, C., Arnold, S. E., Das, S., Edlow, B. L., Alexander, D. C., Golland, P. and Fischl, B. (2023), 'Synthsr: A public ai tool to turn heterogeneous clinical brain scans into high-resolution t1-weighted images for 3d morphometry', *Science advances* **9**(5), eadd3607.
- Iglesias, J. E., Billot, B., Balbastre, Y., Tabari, A., Conklin, J., González, R. G., Alexander, D. C., Golland, P., Edlow, B. L., Fischl, B. et al. (2021), 'Joint super-resolution and synthesis of 1 mm isotropic mp-rage volumes from clinical mri exams with scans of different orientation, resolution and contrast', *Neuroimage* **237**, 118206.
- Kalaitzakis, M., Pearce, R. and Gentleman, S. (2009), 'Clinical correlates of pathology in the claustrum in parkinson's disease and dementia with lewy bodies', *Neuroscience letters* **461**(1), 12–15.
- Kang, S. S., Bodenheimer, J. and Butler, T. (2020), 'A comprehensive protocol for manual segmentation of the human claustrum and its sub-regions using high-resolution mri', *arXiv preprint arXiv:2010.06423*.
- Kapakin, S. (2011), 'The claustrum: three-dimensional reconstruction, photorealistic imaging, and stereotactic approach', *Folia morphologica* **70**(4), 228–234.
- Kirchhoff, Y., Rokuss, M. R., Roy, S., Kovacs, B., Ulrich, C., Wald, T., Zenk, M., Vollmuth, P., Kleesiek, J., Isensee, F. et al. (2024), 'Skeleton recall loss for connectivity conserving and resource efficient segmentation of thin tubular structures', *arXiv preprint arXiv:2404.03010*.
- Koubeissi, M. Z., Bartolomei, F., Beltagy, A. and Picard, F. (2014), 'Electrical stimulation of a small brain area reversibly disrupts consciousness', *Epilepsy & Behavior* **37**, 32–35.
- Krimmel, S. R., White, M. G., Panicker, M. H., Barrett, F. S., Mathur, B. N. and Seminowicz, D. A. (2019), 'Resting state functional connectivity and cognitive task-related activation of the human claustrum', *Neuroimage* **196**, 59–67.
- Li, H., Menegaux, A., Schmitz-Koep, B., Neubauer, A., Bäuerlein, F. J., Shit, S., Sorg, C., Menze, B. and Hedderich, D. (2021), 'Automated claustrum segmentation in human brain mri using deep learning', *Human Brain Mapping* **42**(18), 5862–5872.
- Lin, M., Weng, N., Mikolaj, K., Bashir, Z., Svendsen, M. B., Tolsgaard, M. G., Christensen, A. N. and Feragen, A. (2024), Shortcut learning in medical image segmentation, in 'International Conference on Medical Image Computing and Computer-Assisted Intervention', Springer, pp. 623–633.
- Lüsebrink, F., Sciarra, A., Mattern, H., Yakupov, R. and Speck, O. (2017), 'T1-weighted in vivo human whole brain mri dataset with an ultrahigh isotropic resolution of 250  $\mu\text{m}$ ', *Scientific data* **4**(1), 1–12.
- Madden, M. B., Stewart, B. W., White, M. G., Krimmel, S. R., Qadir, H., Barrett, F. S., Seminowicz, D. A. and Mathur, B. N. (2022), 'A role for the claustrum in cognitive control', *Trends in cognitive sciences* **26**(12), 1133–1152.
- Mai, J. K., Majtanik, M. and Paxinos, G. (2015), *Atlas of the human brain*, Academic Press.
- Malone, I. B., Cash, D., Ridgway, G. R., MacManus, D. G., Ourselin, S., Fox, N. C. and Schott, J. M. (2013), 'Miriad—public release of a multiple time point alzheimer's mr imaging dataset', *NeuroImage* **70**, 33–36.
- Marques, J. P., Kober, T., Krueger, G., van der Zwaag, W., Van de Moortele, P.-F. and Gruetter, R. (2010), 'Mp2rage, a self bias-field corrected sequence for improved segmentation and t1-mapping at high field', *Neuroimage* **49**(2), 1271–1281.
- Mathur, B. N. (2014), 'The claustrum in review', *Frontiers in systems neuroscience* **8**, 48.
- Meletti, S., Slonkova, J., Mareckova, I., Monti, G., Specchio, N., Hon, P., Giovannini, G., Marcan, V., Chiari, A., Krupa, P. et al. (2015), 'Claustrum damage and refractory status epilepticus following febrile illness', *Neurology* **85**(14), 1224–1232.
- Milardi, D., Bramanti, P., Milazzo, C., Finocchio, G., Arrigo, A., Santoro, G., Trimarchi, F., Quartarone, A., Anastasi, G. and Gaeta, M. (2015), 'Cortical and subcortical connections of the human claustrum revealed in vivo by constrained spherical deconvolution tractography', *Cerebral Cortex* **25**(2), 406–414.
- Naghavi, H. R., Eriksson, J., Larsson, A. and Nyberg, L. (2007), 'The claustrum/insula region integrates conceptually related sounds and pictures', *Neu-*

- rosience letters* **422**(1), 77–80.
- Neubauer, A., Li, H. B., Wendt, J., Schmitz-Koep, B., Menegaux, A., Schinz, D., Menze, B., Zimmer, C., Sorg, C. and Hedderich, D. M. (2022), 'Efficient claustrum segmentation in t2-weighted neonatal brain mri using transfer learning from adult scans', *Clinical Neuroradiology* **32**(3), 665–676.
- Nikolenko, V. N., Rizaeva, N. A., Beeraka, N. M., Oganesyanyan, M. V., Kudryashova, V. A., Dubovets, A. A., Borminskaya, I. D., Bulygin, K. V., Sinelnikov, M. Y. and Aliev, G. (2021), 'The mystery of claustral neural circuits and recent updates on its role in neurodegenerative pathology', *Behavioral and brain functions* **17**, 1–10.
- Patru, M. C. and Reser, D. H. (2015), 'a new perspective on delusional states—evidence for claustrum involvement', *Frontiers in psychiatry* **6**, 158.
- Perlaki, G., Horvath, R., Nagy, S. A., Bogner, P., Doczi, T., Janszky, J. and Orsi, G. (2017), 'Comparison of accuracy between fsl's first and freesurfer for caudate nucleus and putamen segmentation', *Scientific reports* **7**(1), 2418.
- Redouté, J., Stoléru, S., Grégoire, M.-C., Costes, N., Cinotti, L., Lavenne, F., Le Bars, D., Forest, M. G. and Pujol, J.-F. (2000), 'Brain processing of visual sexual stimuli in human males', *Human brain mapping* **11**(3), 162–177.
- Remedios, R., Logothetis, N. K. and Kayser, C. (2010), 'Unimodal responses prevail within the multisensory claustrum', *Journal of Neuroscience* **30**(39), 12902–12907.
- Remedios, R., Logothetis, N. K. and Kayser, C. (2014), 'A role of the claustrum in auditory scene analysis by reflecting sensory change', *Frontiers in systems neuroscience* **8**, 44.
- Reuter, M., Schmansky, N. J., Rosas, H. D. and Fischl, B. (2012), 'Within-subject template estimation for unbiased longitudinal image analysis', *Neuroimage* **61**(4), 1402–1418.
- Rodríguez-Vidal, L., Alcauter, S. and Barrios, F. A. (2024), 'The functional connectivity of the human claustrum, according to the human connectome project database', *Plos one* **19**(4), e0298349.
- Ronneberger, O., Fischer, P. and Brox, T. (2015), U-net: Convolutional networks for biomedical image segmentation, in 'Medical image computing and computer-assisted intervention—MICCAI 2015: 18th international conference, Munich, Germany, October 5–9, 2015, proceedings, part III 18', Springer, pp. 234–241.
- Sener, R. (1993), 'The claustrum on mri: normal anatomy, and the bright claustrum as a new sign in wilson's disease', *Pediatric radiology* **23**, 594–596.
- Sener, R. N. (1998), 'Lesions affecting the claustrum', *Computerized medical imaging and graphics* **22**(1), 57–61.
- Silva, G., Jacob, S., Melo, C., Alves, D. and Costa, D. (2018), 'Claustrum sign in a child with refractory status epilepticus after febrile illness: why does it happen?', *Acta Neurologica Belgica* **118**, 303–305.
- Sitte, H. H., Pifl, C., Rajput, A. H., Hörtnagl, H., Tong, J., Lloyd, G. K., Kish, S. J. and Hornykiewicz, O. (2017), 'Dopamine and noradrenaline, but not serotonin, in the human claustrum are greatly reduced in patients with parkinson's disease: possible functional implications', *European Journal of Neuroscience* **45**(1), 192–197.
- Smith, J. B., Lee, A. K. and Jackson, J. (2020), 'The claustrum', *Current Biology* **30**(23), R1401–R1406.
- Smith, J. B., Watson, G. D., Liang, Z., Liu, Y., Zhang, N. and Alloway, K. D. (2019), 'A role for the claustrum in salience processing?', *Frontiers in neuroanatomy* **13**, 64.
- Smythies, J., Edelman, L. and Ramachandran, V. (2012), 'Hypotheses relating to the function of the claustrum', *Frontiers in integrative neuroscience* **6**, 53.
- Terem, A., Gonzales, B. J., Peretz-Rivlin, N., Ashwal-Fluss, R., Bleistein, N., del Mar Reus-Garcia, M., Mukherjee, D., Groysman, M. and Citri, A. (2020), 'Claustral neurons projecting to frontal cortex mediate contextual association of reward', *Current Biology* **30**(18), 3522–3532.
- Tian, F., Tu, S., Qiu, J., Lv, J., Wei, D., Su, Y. and Zhang, Q. (2011), 'Neural correlates of mental preparation for successful insight problem solving', *Behavioural brain research* **216**(2), 626–630.
- Torgerson, C. M., Irimia, A., Goh, S. M. and Van Horn, J. D. (2015), 'The dti connectivity of the human claustrum', *Human brain mapping* **36**(3), 827–838.
- Venneri, A. and Shanks, M. (2014), 'The claustrum and alzheimer's disease', *The claustrum* pp. 263–275.
- Volz, K. G., Schooler, L. J. and von Cramon, D. Y. (2010), 'It just felt right: The neural correlates of the fluency heuristic', *Consciousness and Cognition* **19**(3), 829–837.
- Wada, J. A. and Kudo, T. (1997), 'Involvement of the claustrum in the convulsive evolution of temporal limbic seizure in feline amygdaloid kindling', *Electroencephalography and clinical neurophysiology* **103**(2), 249–256.
- Wegiel, J., Flory, M., Kuchna, I., Nowicki, K., Ma, S. Y., Imaki, H., Wegiel, J., Frackowiak, J., Kolecka, B. M., Wierzbica-Bobrowicz, T. et al. (2015), 'Neuronal nucleus and cytoplasm volume deficit in children with autism and volume increase in adolescents and adults', *Acta neuropathologica communications* **3**, 1–17.
- White, M. G., Panicker, M., Mu, C., Carter, A. M., Roberts, B. M., Dharmasri, P. A. and Mathur, B. N. (2018), 'Anterior cingulate cortex input to the claustrum is required for top-down action control', *Cell reports* **22**(1), 84–95.
- Yamamoto, R., Iseki, E., Murayama, N., Minegishi, M., Marui, W., Togo, T., Katsuse, O., Kosaka, K., Kato, M., Iwatsubo, T. et al. (2007), 'Correlation in lewy pathology between the claustrum and visual areas in brains of dementia with lewy bodies', *Neuroscience letters* **415**(3), 219–224.
- Zhang, X., Hannesson, D. K., Saucier, D. M., Wallace, A. E., Howland, J. and Corcoran, M. E. (2001), 'Susceptibility to kindling and neuronal connections of the anterior claustrum', *Journal of Neuroscience* **21**(10), 3674–3687.